

Atomic Layer Deposition of Cobalt(II) Oxide Thin Films from $\text{Co}(\text{BTSA})_2(\text{THF})$ and H_2O

Running title: Atomic Layer Deposition of Cobalt(II) Oxide

Running Authors: Iivonen et al.

Tomi Iivonen^{a)}, Mikko Kaipio, Timo Hatanpää

Department of Chemistry, University of Helsinki, P.O. Box 55, FI-00014 Helsinki, Finland

Kenichiro Mizohata, Kristoffer Meinander, Jyrki Räisänen

Department of Physics, University of Helsinki, P.O. Box 43, FI-00014 Helsinki, Finland

Jiyeon Kim

Inorganic Materials Chemistry, Faculty of Chemistry and Biochemistry, Ruhr-University Bochum, Universitätsstr. 150, 44801 Bochum, Chemistry

Mikko Ritala, Markku Leskelä^{b)}

Department of Chemistry, University of Helsinki, P.O. Box 55, FI-00014 Helsinki, Finland

^{a)} Electronic mail: tomi.iivonen@helsinki.fi

^{b)} Electronic mail: markku.leskela@helsinki.fi

In this work, we have studied the applicability of $\text{Co}(\text{BTSA})_2(\text{THF})$ (BTSA = bis(trimethylsilyl)amido) (THF = tetrahydrofuran) in atomic layer deposition (ALD) of cobalt oxide thin films. When adducted with THF, the resulting $\text{Co}(\text{BTSA})_2(\text{THF})$ showed good volatility and could be evaporated at 55 °C, which enabled film deposition in the temperature range of 75–250 °C. Water was used as the co-reactant, which led to the formation of Co(II) oxide films. The saturative growth mode characteristic to ALD was confirmed with respect to both precursors at deposition temperatures of 100 and 200 °C. According to grazing incidence X-ray diffraction measurements, the films contain both cubic rock salt and hexagonal wurtzite phases of CoO. X-ray photoelectron

spectroscopy measurements confirmed that the primary oxidation state of cobalt in the films is +2. Film composition was analyzed using time-of-flight elastic recoil detection analysis (ToF-ERDA), which revealed the main impurities in the films to be H and Si. The Si impurities originate from the BTSA ligand and increased with increasing deposition temperature, which indicates that $\text{Co}(\text{BTSA})_2(\text{THF})$ is best suited for low temperature deposition. To gain insight to the surface chemistry of the deposition process, an *in-situ* reaction mechanism study was conducted using quadrupole mass spectroscopy and quartz crystal microbalance techniques. Based on the *in-situ* experiments, it can be concluded that film growth occurs via a ligand exchange mechanism.

I. INTRODUCTION

Cobalt forms several oxygen containing compounds, including oxides, hydroxides and oxyhydroxides.¹ These materials, especially in nanostructured form, find use in emerging technologies related to energy production and storage, such as (photo)electrochemical water splitting²⁻⁵ and lithium ion batteries.⁶⁻⁸ Regarding these applications, a control of the oxidation state of cobalt is of great importance, as cobalt monoxide (CoO) and the mixed valence cobalt(II,III) oxide (Co_3O_4) differ from one another both structurally and electronically. In addition to controlling the oxidation state of cobalt, the amount of impurities present in these materials should be minimized, as they can affect the aforementioned structural and electronic properties. In the bulk form, pure CoO is a charge transfer insulator⁹ that crystallizes in the rock salt form.¹⁰ In nanocrystalline form, cobalt monoxide can crystallize also in the cubic zinc blende and

hexagonal wurtzite forms.¹⁰⁻¹² Co_3O_4 on the other hand, is a p-type semiconductor^{13,14} that assumes the spinel-type crystal structure.¹⁵ While the bulk properties related to the structure and electronic properties of cobalt oxides are well defined, the surface chemistry of these materials is more complex. For example, both CoO and Co_3O_4 can undergo surface hydroxylation upon exposure to moisture^{1,3,16} and at elevated temperatures, the hydroxides can decompose back to oxides.¹ Additionally, the surface of the lower valence CoO is readily oxidized to Co^{3+} in ambient conditions, which makes obtaining pure cobalt monoxide samples difficult.¹⁷ Due to the challenges associated with the oxidation state and surface chemistry of cobalt oxides, controllable and repeatable methods should be explored for their fabrication.

In this study, we have used the atomic layer deposition (ALD) technique for creating nanocrystalline cobalt(II) oxide thin films. ALD is an advanced variant of the chemical vapor deposition (CVD) method and is based on controlled and self-limiting surface reactions between alternately supplied film-forming precursors.¹⁸ In recent years, ALD has been gaining increasing attention in the field of nanotechnology as it can be used to deposit uniform films of oxides, sulfides, nitrides, fluorides and metals with unmatched conformality and thickness control in the sub-nanometer range.¹⁹ In a typical ALD process for metal oxides, thin films are deposited using a combination of two film-forming precursors, i.e. the metal containing precursor, and the oxygen source. The metal precursors include halides, alkoxides, β -diketonates and other, more complex metalorganic or organometallic compounds whereas the most common oxygen sources are water vapor, oxygen plasma and ozone.²⁰ A majority of the reported ALD cobalt oxide processes rely on the use of either oxygen plasma or ozone to remove the ligands of

the metalorganic or organometallic cobalt precursors.^{21–29} Due to the high oxidative power of O₂ plasma and O₃, the ligand combustion approach leads to oxidation of cobalt to Co³⁺ and the subsequent formation of Co₃O₄ films. In order to deposit CoO films, the use of highly oxidizing co-reactants should therefore be avoided. Reports on ALD of CoO are fewer and they are all based on the use of metalorganic cobalt precursors where the oxidation state of Co is +2 and that are reactive towards water.^{30–32} In the case of Co(ⁱPrAMD)₂ (ⁱPrAMD = N,N'-di-isopropylacetamidinate), CoO films have been deposited at 170–180 °C³¹ and at 250 °C³⁰, but the saturative growth mode characteristic to ALD processes was not confirmed in these reports. In a more recent study on ALD of CoO films, a cobalt(II) chloride diamine adduct CoCl₂(TMEDA), (TMEDA = N,N,N',N'-tetramethyl-ethylenediamine) and H₂O were used to deposit stoichiometric and crystalline cobalt monoxide films at 225–300 °C.³² The drawback CoCl₂(TMEDA) is, however, that it requires a relatively high source temperature of 170 °C, which effectively limits the deposition temperature range to 200 °C and above.

In order to explore the possibility to deposit cobalt monoxide thin films at low temperatures, we have studied the combination of a silylamide cobalt(II) precursor, Co(BTSA)₂(THF) (THF = tetrahydrofuran) (BTSA = bis(trimethylsilyl)amido) and water vapor in ALD. The BTSA ligand can be used to volatilize many transition metals, including Cr, Mn, Fe, Co, Cu, Sn and Ge³³ and therefore presents interesting opportunities for gas phase deposition of thin films containing the said elements. Previous reports of ALD that employ homoleptic metal BTSA precursors include the deposition of lithium silicate,^{34,35} lithium niobate,³⁶ bismuth oxide,³⁷ iron oxide³⁸, tin oxide³⁹, lanthanum oxide^{40–43}, lanthanum aluminum oxide⁴⁴ and praseodymium oxide.⁴³

When metal BTSA precursors are used in ozone based ALD, the resulting films are a mixture of oxide and silicate due to the formation of non-volatile –O–Si–O– moieties in the films.^{34,35,39} Moreover, heteroleptic metal precursors containing the BTSA ligand have been used in ALD of hafnium oxide/silicate⁴⁵, copper⁴⁶ and also gold thin films⁴⁷, which is a further indication of the potential of the BTSA ligand in ALD chemistry.

In the study reported herein, $\text{Co}(\text{BTSA})_2(\text{THF})$ was synthesized and its volatility was evaluated using thermal gravimetry. $\text{Co}(\text{BTSA})_2(\text{THF})$ was found to volatilize *in vacuo* already at 55 °C and thus proved to be promising for deposition of cobalt oxide films. Deposition experiments were carried out within a temperature window of 75–250 °C. The lower and higher limits of the deposition temperature window were defined by the evaporation temperature and the reductive decomposition onset of the cobalt precursor, respectively. In addition to the saturation studies and film characterization, *in-situ* reaction mechanism studies were conducted using quartz crystal microbalance (QCM) and quadrupole mass spectroscopy (QMS) techniques.⁴⁸ The *in-situ* studies show that the film growth occurs via a ligand exchange mechanism. However, based on the compositional analysis of the films and the *in-situ* studies, minor thermal decomposition or condensation of the cobalt precursor are affecting the film growth as well.

II. EXPERIMENT

A. Precursor synthesis

Synthesis and handling of air and moisture sensitive chemicals were done under rigorous exclusion of air and moisture using standard Schlenk and glove box techniques.

Anhydrous CoCl_2 (99%, Aldrich) and $\text{Li}(\text{BTSA})$ (97%, Aldrich) were used as received. THF was freshly distilled from sodium benzophenone ketyl. Thermogravimetric analysis was performed using a Mettler Toledo STAR^e system equipped with a TGA850 thermobalance. The measurements were done at atmospheric pressure using N_2 (50 mL/min) as the purge gas. The heating rate was $10\text{ }^\circ\text{C}/\text{min}$, and the sample size was 10 ± 1 mg. Melting points were taken from single-differential thermal analysis (SDTA) data measured by the thermobalance. Synthesis of $\text{Co}(\text{BTSA})_2(\text{THF})$ was done modifying a procedure found in the literature.⁴⁹ In short, 3.42 g CoCl_2 (26.34 mmol) was weighed into a 300 ml Schlenk bottle. 50 ml of THF was added. 8.82 g of $\text{Li}(\text{BTSA})$ (52.71 mmol) dissolved in 100 ml of THF was added dropwise to the stirred suspension. After stirring the resulting solution for 2 hours at RT, excess THF was evaporated away. The resulting dark green solid was transferred to a sublimation apparatus and sublimed at $80\text{--}95\text{ }^\circ\text{C}$ / 0.4 mbar. Yield of the dark green product was 7.61 g (63.9%). m.p. $69.5\text{--}72\text{ }^\circ\text{C}$.

B. Film deposition

Cobalt oxide films were deposited using a commercial, hot-wall F-120 ALD reactor (ASM Microchemistry Ltd.) operated in the cross-flow configuration.⁵⁰ Nitrogen (99.999 %, $\text{O}_2 \leq 5$ ppm, $\text{H}_2\text{O} \leq 5$ ppm, AGA) was used as carrier and purging gas at a flow rate of 400 sccm. The reactor pressure during the depositions was approximately 10 mbar. Native oxide terminated Si (100) (Okmetic Oy, Vantaa, Finland) and soda lime glass (SLG) cut to $5\times 5\text{ cm}^2$ squares were used as substrates. The silicon substrates were used as received whereas the glass substrates were cleaned using ultrasonication in successive baths of an alkaline detergent, ethanol and deionized water. The cobalt

precursor, $\text{Co}(\text{BTSA})_2(\text{THF})$, was evaporated from an open glass boat held inside the reactor at 55 °C. Water vapor was introduced to the ALD reactor through needle and solenoid valves from an external reservoir held at room temperature. Films were deposited in a temperature range of 75–250 °C.

C. *In-situ* reaction mechanism studies

The *in-situ* measurements were performed using a modified F-120 ALD reactor equipped with a quartz crystal microbalance (QCM) and a quadrupole mass spectrometer (QMS).⁵¹ In short, the reactor consists of two chambers, the deposition chamber where the QCM is located, and the QMS chamber. The deposition chamber also contains a set of large area SLG substrates in order to obtain a sufficient amount of gaseous reaction byproducts for the QMS analyzer. The combined area of the SLG substrates and reactor walls is approximately 3500 cm². The two chambers are connected through a 100 μm orifice. The base pressure in the deposition chamber is approximately 10 mbar whereas the pressure in the QMS chamber is in the order of 10⁻⁵ mbar. The pressure difference is obtained by differential pumping through the orifice by using turbomolecular and mechanical pumps. The gaseous species are analyzed with a Hiden HAL/3F 501 RC QMS equipped with a Faraday cup detector. Ionization energy of 70 eV was used in the analyses. Mass changes in the deposition chamber were monitored with a Maxtek TM 400 QCM operated at a sampling rate of 20 Hz. Nitrogen (99.999 %, O₂ ≤ 5 ppm, H₂O ≤ 5 ppm, AGA) was used as carrier and purging gases. D₂O (99.96 % D, Eurisotop) was used instead of H₂O in all of the *in-situ* measurements, as deuterium helps to identify byproducts of ligand exchange reactions with QMS.

D. Film characterization

All characterizations were done using films deposited on native oxide terminated Si(100) substrates unless otherwise noted. Film thicknesses were measured with ellipsometry using a Film Sense FS-1 Multi-Wavelength instrument. Film thicknesses were calculated using the Cauchy model. The origin of the error bars in data related to film thickness is the fit error of the Cauchy model. In addition, the thicknesses of certain films were measured using X-ray reflectivity (XRR) and UV-Vis spectroscopy in reflectance mode. The XRR measurements were performed using a PANalytical X'Pert Pro MPD diffractometer and the UV-Vis measurements with a Hitachi U2000 spectrophotometer. Film thickness was calculated from the UV-Vis reflectance data using the ThinFilm software package.⁵² For 50 nm thick films (as measured with XRR), ellipsometry and UV-Vis measurements resulted in thickness values of 50 ± 1 nm, proving that the optical methods could be used for accurate determination of film thickness in this range.

Film structure was determined via grazing incidence X-ray diffraction (GI-XRD) measurements using a Rigaku SmartLab X-ray diffractometer. The diffractograms were collected using Cu K α radiation ($\lambda = 1.54 \text{ \AA}$) at an incident angle of 1° .

Film morphology was studied with atomic force microscopy (AFM). The AFM images were collected with a Veeco V Multimode instrument equipped with a Nanoscope V controller. The imaging was performed at a scan rate of 1 Hz in the intermittent contact mode (tapping mode) in air using Si probes with a nominal tip radius of < 10 nm (Bruker). The images were flattened and planefitted in order to remove artefacts caused

by scanner bow and sample tilt. Surface roughness of the films was calculated as average root mean square values (R_q) from $2 \times 2 \mu\text{m}^2$ images.

The composition of the films was determined with time-of-flight elastic recoil detection analysis (ToF-ERDA) using an ion-beam setup described in full elsewhere.⁵³ The cobalt oxide films analyzed with ToF-ERDA were deposited on 50 nm thick ALD TiO_2 films made using the $\text{Ti}(\text{OMe})_4 + \text{H}_2\text{O}$ process at 300°C ⁵⁴ to avoid disturbance from the silicon substrate while quantifying the level of Si impurities originating from the BTSA ligands.

The chemical state of cobalt and oxygen in the films was determined using X-ray photoelectron spectroscopy (XPS). The XPS measurements were done in a system consisting of an Argus spectrometer (Omicron NanoTechnology GmbH) and a standard Mg source ($K\alpha$ line, photon energy of 1253.6 eV). Binding energies were calibrated using the C 1s peak of ambient hydrocarbons found at 284.8 eV. No sputtering was performed on the samples. Peak fitting and data analysis was done using the CasaXPS software package (www.casaxps.com).

III. RESULTS AND DISCUSSION

A. *Precursor properties*

$\text{Co}(\text{BTSA})_2(\text{THF})$ was synthesized using a simple literature metathesis reaction between CoCl_2 and LiBTSA in THF.⁴⁹ In $\text{Co}(\text{BTSA})_2(\text{THF})$, THF acts as an adduct forming ligand and coordinates to cobalt in order to compensate for the coordinative unsaturation of the metal center. The coordinative bond between Co and THF in

Co(BTSA)₂(THF) is surprisingly strong and cannot be broken by refluxing in solvent with a high boiling point, i.e. toluene or xylene. Heating Co(BTSA)₂(THF) under vacuum does not lead to removal of THF either but the compound sublimes intact, instead. If the synthesis is done in Et₂O instead of THF, the dimeric [Co(BTSA)₂]₂ can be obtained.⁴⁹ In the dimeric version of Co(BTSA)₂, two of the trimethylsilylamide ligands act as bridging η²-ligands between two cobalt atoms.

Prior to film deposition experiments, the thermal properties of both Co(BTSA)₂(THF) and the dimeric [Co(BTSA)₂]₂ were evaluated using thermogravimetric analysis (TGA). Both versions of Co(BTSA)₂ were found to volatilize in a single step which shows that neither of the compounds undergoes detrimental decomposition upon heating in oxygen and moisture free conditions (Fig. 1). Residual masses of the two cobalt precursors were in the range of 3–4 %. The residues are likely to form in a reaction between the cobalt precursor and ambient moisture when loading the sample to the TGA instrument.

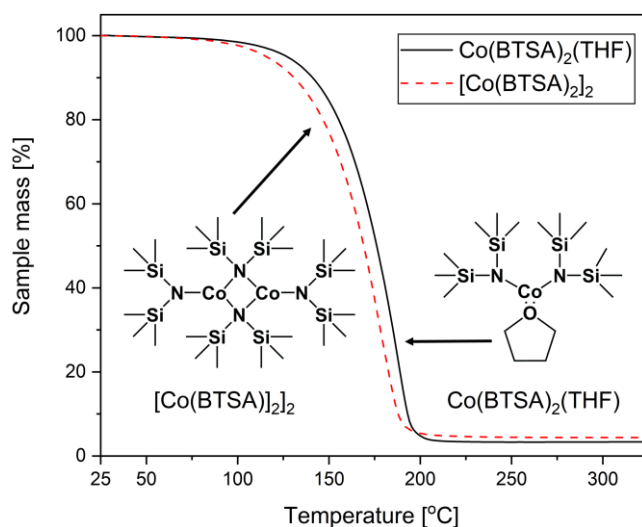


FIG. 1. (Color online) TGA graphs Co(BTSA)₂(THF) and [Co(BTSA)₂]₂ as measured under an N₂ gas flow. The molecular structures of the precursors are shown as insets.

According to TGA performed at atmospheric pressure, the dimeric $[\text{Co}(\text{BTSA})_2]_2$ evaporates at a slightly lower temperature than the monomeric $\text{Co}(\text{BTSA})_2(\text{THF})$. However, in ALD conditions, i.e. a pressure of approximately 10 mbar, $\text{Co}(\text{BTSA})_2(\text{THF})$ could be evaporated at a temperature of 55 °C, whereas $[\text{Co}(\text{BTSA})_2]_2$ required a source temperature of 70 °C. Melting points of $\text{Co}(\text{BTSA})_2(\text{THF})$ and $[\text{Co}(\text{BTSA})_2]_2$ were measured to be 69.5–72 °C and 94–98.5 °C respectively, which indicates that both precursors are solid at their respective ALD source temperatures. As $\text{Co}(\text{BTSA})_2(\text{THF})$ exhibited better volatility *in vacuo*, it was used in all further film deposition experiments in order to allow a wider deposition temperature range.

B. Film deposition

Film deposition was studied in a temperature range of 75–250 °C. The growth per cycle value (GPC) of the cobalt oxide films was found to have a strong dependence on the deposition temperature (Fig. 2)

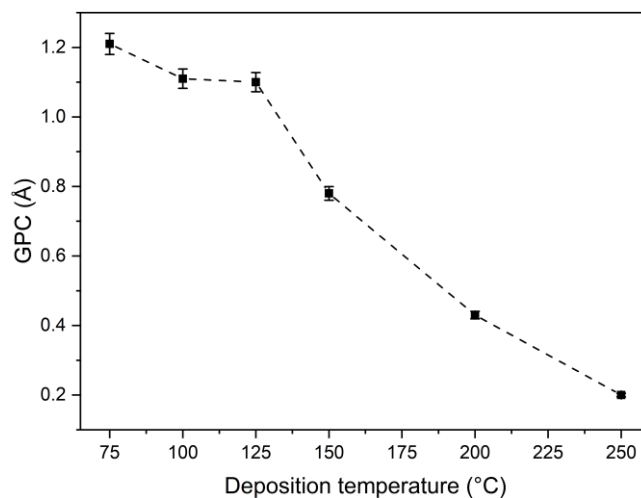


FIG. 2. Effect of deposition temperature to GPC of the cobalt oxide films. The dashed line connecting the data points is to guide the reader's eye.

At the lowest deposition temperature studied, 75 °C, the films grew with a GPC of 1.2 Å. Upon increasing the deposition temperature to 100 and 125 °C, the GPC leveled to a constant 1.1 Å. The higher GPC at 75 °C can be explained by a higher coverage of surface –OH groups, or even the formation of Co(OH)₂ intermediates, which both can increase the adsorption density of the cobalt precursor. Deposition experiments done at 150, 200 and 250 °C resulted in GPC values of 0.78, 0.43 and 0.20 Å, respectively. Attempts to deposit cobalt oxide films at 275 °C led to an accumulation of a metallic solid in the hot end of the precursor tube of Co(BTSA)₂(THF), indicating that the cobalt precursor was undergoing reductive thermal decomposition. Therefore, 250 °C was chosen as the upper limit for the deposition experiments.

Regarding the decreasing GPC with increasing deposition temperature, similar results have been reported also with other water-based metal oxide ALD processes using metal precursors with BTSA-ligands, namely Fe(BTSA)₂³⁸, Sn(BTSA)₂³⁹ and HfCl₂(BTSA)₂⁴⁵. The authors of the HfCl₂(BTSA)₂ + H₂O ALD process suggested that the decrease in GPC at higher temperatures is due to surface dehydroxylation, which diminishes the adsorption of the metal precursor.⁴⁵ In the case of the tin oxide process, it was suggested that the decreasing GPC at higher deposition temperatures is due to reactions between protonated BTSA ligands that form as byproducts, and surface hydroxyl groups.³⁹ In this mechanism, the protonated BTSA ligand undergoes bond rearrangement which results in formation of ammonia and unreactive surface O–SiMe₃ groups that inhibit further film growth. The amount of silicon impurities in the SnO films

was reported to increase with increasing deposition temperature which can also point out to that the metal precursor is undergoing partial decomposition.

Film growth was found to saturate at deposition temperatures of 100 and 200 °C using precursor pulses of identical lengths, i.e. 1.5 s pulses for the cobalt precursor (Fig. 3a) and 2.0 s pulses for water (Fig. 3b). At 100 °C, purge times of up to 8 s were required to produce visually uniform films over the 5×5 cm² substrates whereas at the deposition temperature of 200 °C, purge times of 2 s were sufficient. The requirement for long purge times is a well-known in low-temperature thermal ALD, especially when water is used as a co-reactant.⁵⁵ The phenomenon is attributed to the low vapor pressure of water and also its tendency to adsorb to both on the film surface and to the walls of the reaction chamber.¹⁸

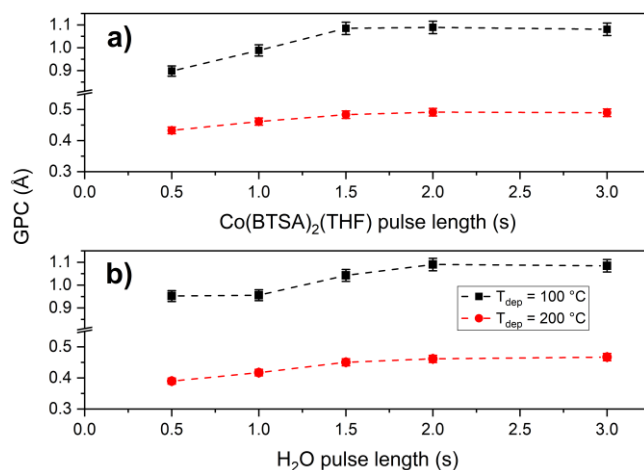


FIG. 3. Effect of pulse lengths of a) Co(BTSA)₂(THF) and b) H₂O of GPC of the cobalt oxide films deposited at 100 and 200 °C. Purge times were 8 s at 100 °C and 2 s at 200 °C for both precursors. The dashed lines connecting the data points are to guide the reader's eye.

The dependence between the number of deposition cycles and film thickness was also studied at deposition temperatures of 100 and 200 °C. At these deposition temperatures, thicknesses of the cobalt oxide films were found to be linearly dependent on the number of applied deposition cycles (Fig. 4). No major nucleation delay effect was present at either 100 or 200 °C, as expected for oxide on oxide growth.¹⁸

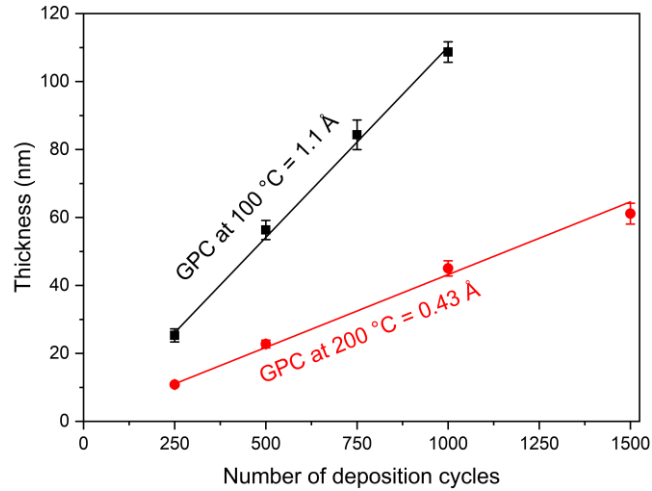


FIG. 4. Relationship between film thickness and number of deposition cycles at 100 and 200 °C. The GPC values have been calculated from linear fits of the data points (solid lines). The R^2 values describing the goodness of the fits are 0.99431 and 0.99789 for deposition temperatures of 100 and 200 °C, respectively.

C. Film characterization

X-ray diffraction measurements of cobalt oxide films were performed in the grazing incidence (GI) geometry. The GI-XRD measurements revealed that the films crystallize as a mixture of the cubic rock salt and hexagonal wurtzite polymorphs of cobalt monoxide (Fig. 5), which is characteristic to nanostructured CoO.³² The existence of the two different polymorphs in the same films complicates the phase analysis, as the

2θ diffraction angles of the (111) plane of the cubic rock salt phase of CoO at 37.0° and the (101) plane of the hexagonal wurtzite phase of CoO at 37.1° are not easily distinguished from each other due to peak broadening.

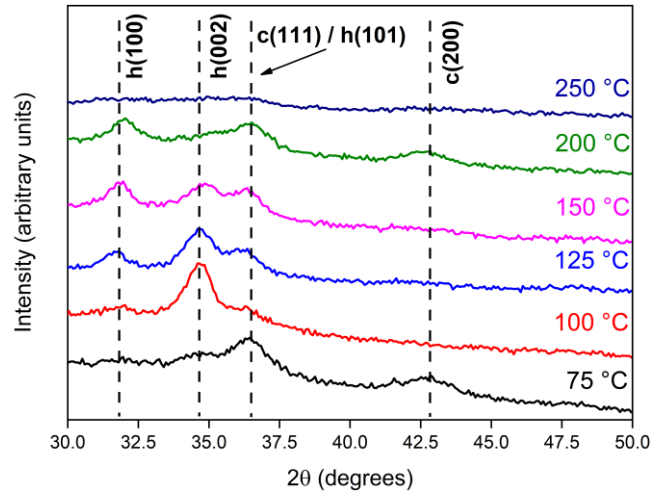


FIG. 5. GI-XRD scans of 50 nm thick cobalt oxide films deposited at 75–250 °C.

In addition to the peak broadening, all diffractions were of low intensity. We assign the peak broadening to originate from small crystallite size. The low intensity of the diffractions, on the other hand, may indicate that the films are not fully crystalline, but partially amorphous. Films deposited at 75 °C were characterized by a weak and broad reflection assignable to the (200) plane of the cubic rock salt phase and a more intensive reflection at 36.5° which can be assigned to either the (111) plane of the cubic rock salt structure or the (101) plane of the hexagonal wurtzite phase. For films deposited at 100 °C, a single reflection belonging to the (002) plane of the hexagonal phase was observed. The diffractograms of films deposited at 125–200 °C consisted of reflections assignable to the (100) and (002) planes of the hexagonal phase and a reflection at 2θ of

36.5°, which can be assigned either to the cubic rock salt phase or the hexagonal wurtzite phase. Based on the intensities of the reflections, the hexagonal phase of CoO is seemingly dominating over the cubic rock salt phase in films obtained at deposition temperatures of 100–200 °C. Films obtained at 250 °C were X-ray amorphous. The amorphous structure of the films deposited at the highest temperature studied in this work is most likely a consequence of increased Si impurity content, as discussed later in the text.

The surface morphology of 50 nm thick films was studied using atomic force microscopy (AFM). A notable difference in the surface morphology and shape of the film-forming grains was observed between the films deposited at 75 °C and those obtained at 100–250 °C (Fig. 6).

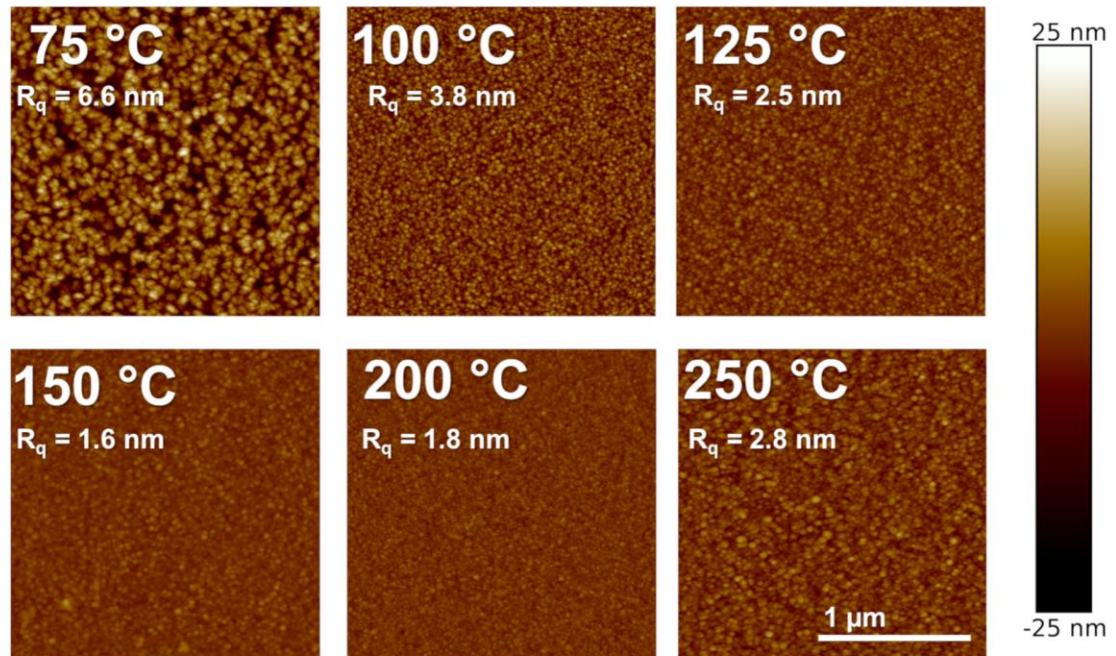


FIG 6. AFM images and R_q values describing the surface roughness of 50 nm thick films deposited at 75–250 °C. The 1 μm scalebar and the height scale apply to all images.

Cobalt oxide films deposited at 75 °C consisted of larger grains and were significantly rougher than those deposited at above 100 °C. The average root-mean-square roughness (R_q) of films deposited at 75 °C was 6.6 nm, which corresponds to approximately 14 % of the film thickness. A conceivable explanation for the high surface roughness observed at for films deposited at 75 °C is that the nucleation density at this temperature is low. This can enable the initial nuclei to grow large before coming to contact with each other, which can cause the surface roughness to increase. At 75 °C, the average grain diameter was 50–120 nm, whereas at deposition temperatures of 100 °C and above, the films consisted of grains approximately 30–60 nm in diameter. In general, films deposited at 100–250 °C were smooth with average root-mean-square surface roughness (R_q) ranging from 1.6 to 3.8 nm, which corresponds to approximately 2–6 % of the film thickness. The low surface roughness of films deposited at 100 °C and above also indicates that the films are partially amorphous.

The chemical composition of the cobalt oxide films was studied using a combination of ToF-ERDA and XPS. ToF-ERDA is an ion-beam technique that can be used to accurately determine the elemental composition of thin films and other structures.^{53,56} Importantly, ToF-ERDA can be used to quantify also light elements, including hydrogen. Elemental compositions of the cobalt oxide films deposited at 75–250 °C as determined using ToF-ERDA are presented in Table 1. High resolution photoelectron spectra of the Co 2p and O 1s regions of the cobalt oxide films deposited at 100 and 200 °C are presented in Fig. 7. The main impurity element found in films deposited at all temperatures was hydrogen at approximately 12–19 at-% (Table 1). Other impurities in the films were carbon and silicon, which are both present in the BTSA

ligand. According to the ERDA depth profiles, the distribution of the impurities is even throughout the films. Nitrogen impurities were not present or were below the detection limit of < 0.2 at-%. The amount of carbon was approximately 2 at-% in all films, while the Si impurity content increased with increasing deposition temperature, ranging from 1.8 at-% at 75 °C up to 6.4 at-% at 250 °C.

TABLE I. Film composition (atomic-%) for 50 nm thick films deposited at 75–250 °C as determined by using ToF-ERDA.

T_{dep} (°C)	75	100	125	150	200	250
Co	37.6 ± 0.4	38.3 ± 0.4	34.5 ± 0.3	34.0 ± 0.3	33.6 ± 0.4	32.5 ± 0.4
O	46.7 ± 0.5	41.9 ± 0.8	44.0 ± 0.5	41.3 ± 0.7	46.0 ± 0.8	46.7 ± 0.9
C	1.9 ± 0.1	2.1 ± 0.1	2.3 ± 0.1	2.6 ± 0.1	2.1 ± 0.1	2.1 ± 0.2
H	12.1 ± 0.5	15.2 ± 1.5	16.7 ± 0.6	18.7 ± 1.3	13.0 ± 1.4	12.3 ± 1.4
Si	1.8 ± 0.1	2.2 ± 0.1	2.5 ± 0.1	3.3 ± 0.1	5.4 ± 0.2	6.4 ± 0.3
Co:O	0.81	0.91	0.78	0.82	0.73	0.70
Si:C	0.95	1.1	1.1	1.3	2.6	3.1

The data from the XPS measurements were analyzed using the peak fitting parameters published by Biesinger and coworkers.¹⁷ The photoelectron spectra in the Co $2p_{3/2}$ region consisted of two peaks found at 780.7 ± 0.1 and 786.4 ± 0.1 eV, which indicates that the primary oxidation state of cobalt in the films is +2 (Fig. 7a). The binding energy value of 780.7 ± 0.1 eV can be assigned to three different species, namely CoO and $\text{Co}(\text{OH})_2$ in which the oxidation state of cobalt is +2, or CoOOH (Co^{3+}), but the existence of the strong satellite signal at 786.4 ± 0.1 eV confirms that the oxidation state of cobalt in the films is +2.¹⁷ The more intensive peak in the Co 2p region found at 780.7 ± 0.1 eV

shows asymmetry, which we assign to originate from coexistence of CoO and Co(OH)₂ in the films.

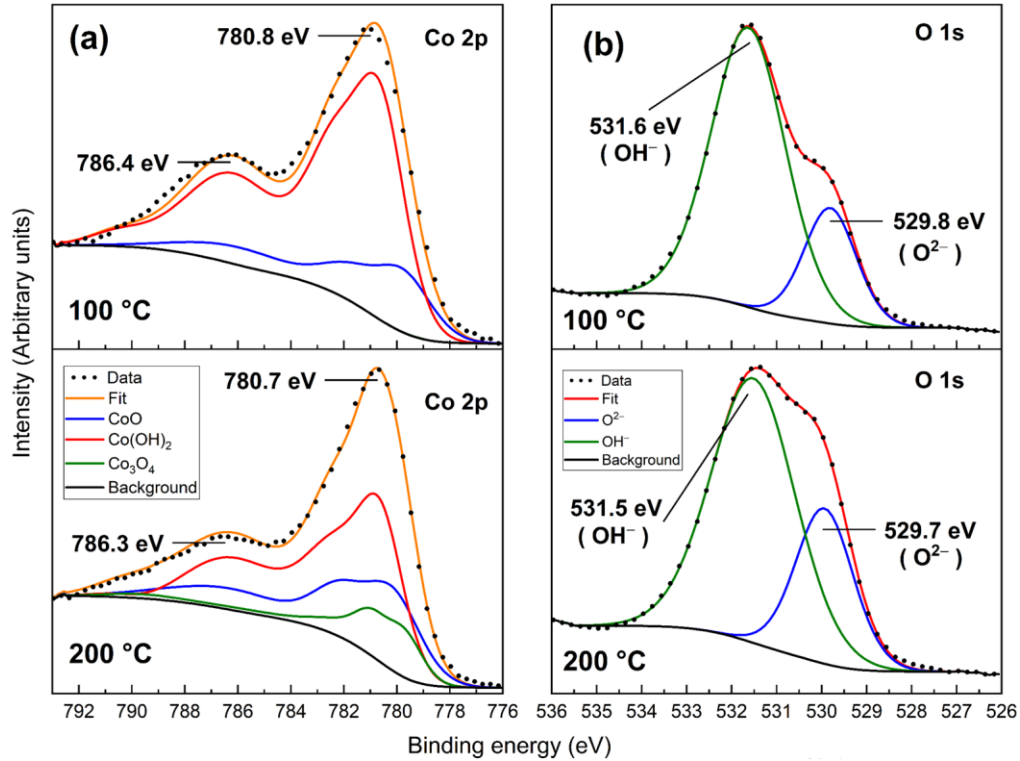


FIG 7. High resolution photoelectron spectra of a) Co 2p and b) O 1s regions for films deposited at 100 and 200 °C.

The O 1s spectra consisted of two peaks found at 529.7 ± 0.1 eV and 531.5 ± 0.1 eV (Fig. 7b.) The peak at the smaller binding energy value, 529.7 ± 0.1 eV, is in good agreement with the literature reference value for the lattice oxide (O^{2-}) of cobalt monoxide (529.79 eV).¹⁷ The peak at the higher binding energy value, 531.5 ± 0.1 eV, is commonly assigned to surface hydroxide (OH^-), hydrated oxide or defective oxide species. As the peak found at 531.5 ± 0.1 eV corresponds to the literature reference value

of CoO (531.37 eV)¹⁷, it can be concluded that the primary oxidation state of cobalt in the films is +2 and that cobalt is not oxidized during the film deposition process.

By combining the information obtained with ToF-ERDA and XPS, we draw the following conclusions on the surface chemistry of the cobalt oxide films and the cobalt precursor, Co(BTSA)₂(THF). As the amount of Si in the films is increasing with increasing deposition temperature, it is clear that Co(BTSA)₂(THF) is not an ideal ALD precursor for cobalt oxide deposition in the sense that the level of impurity atoms has a dependence on deposition temperature. As no nitrogen was detected in the films but silicon was, the Si–N bonds in the BTSA ligands must break and volatile, nitrogen containing byproducts, such as ammonia or its derivatives, are likely to form. Furthermore, as the Si:C ratio is < 1 in films obtained at all deposition temperatures, the Si–C bonds in the BTSA ligands must also break to a certain degree. Therefore, it is plausible that Si exists in the films as –SiMe_x (Me = methyl, x = 1–3) moieties or silicates. As methyl groups are chemically stable, the hydrogen present in the films is likely to originate from two different chemical species, methyl groups and Co(OH)₂. The existence of both Co(OH)₂ and –SiMe_x groups in the films decreases the Co:O ratio to < 1, as seen from Table 1. For Co(OH)₂, the Co:O ratio is 1:2. As for the –SiMe_x groups, they remain in the films because of the strong chemical bond formed between silicon and oxygen atoms and thereby decrease the Co:O ratio in the films.⁵⁷ It should be noted that a Co:O ratio < 1 can also indicate to the formation of the mixed valence cobalt oxide, Co₃O₄ (Co:O = 0.75), but this can be ruled out as the XPS analysis shows that the oxidation state of cobalt in the films is +2. Furthermore, concerning the incorporation of any methyl containing groups in the films, we note that these species are likely to

decrease the adsorption density of both the cobalt precursor and water molecules, which in turn leads to a decrease in the GPC of the process. Another possible factor affecting the GPC is the change in the area density of surface hydroxyl groups, as hydroxyls function as adsorption sites for the cobalt precursor. The thermal decomposition of $\text{Co}(\text{OH})_2$ and $\text{Co}-\text{OH}$ surface groups to CoO has been reported to occur already at temperatures of 130–180 °C and to increase with increasing temperature.^{1,58} From Table 1, it can be seen that the amount of hydrogen in the films starts to decrease after 150 °C. Therefore, it is plausible that the decrease in GPC with increasing deposition temperatures is related to decomposition of surface hydroxyls. However, as discussed earlier, the incorporation of methyl surface groups is most likely contributing to the drop in GPC as well.

D. In-situ reaction mechanism studies

The *in-situ* reaction measurement studies were performed at 100 °C with the following precursor pulsing scheme: 10 D_2O reference pulses + 10 $\text{Co}(\text{BTSA})_2(\text{THF}) / \text{D}_2\text{O}$ cycles + 10 $\text{Co}(\text{BTSA})_2(\text{THF})$ reference pulses. The use of reference pulses has a two-fold informative purpose. A background correction is needed in the reaction by-product analysis: if a measured QMS m/z signal is present during both the reference pulses and the process cycles, the amount of reaction by-product released in a surface reaction is equal to the integrated signal of the precursor pulse during a process cycle minus the integrated signal of the reference pulse. Furthermore, if a QCM measurement

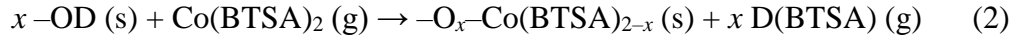
shows an indefinite growth of mass during reference pulses, it is an indication of either physisorption or decomposition of the precursor.

The most likely primary film-forming reaction mechanism in an ALD metal oxide process using water as the oxygen source is 1) a ligand exchange reaction between the metal precursor and surface hydroxyl (–OD) groups, followed by 2) a subsequent ligand exchange between water and the surface groups formed in 1), and the consequent deposition of CoO. In the case of cobalt oxide deposition using Co(BTSA)₂(THF) and D₂O, this is represented by net reaction scheme (1). The THF ligand has been omitted from the following notation for clarity.

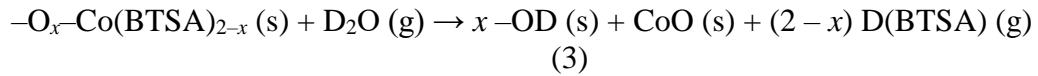
Net reaction:



The first half-reaction during the Co(BTSA)₂(THF) pulse ($0 < x < 2$) is:

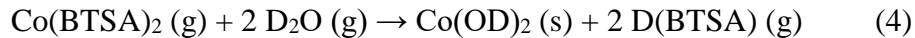


The second half-reaction during the D₂O pulse is:



The compositional analysis results show a significant amount of hydrogen in the films (Table 1). This could be explained by a secondary reaction mechanism, which is a ligand exchange that deposits cobalt(II)hydroxide:

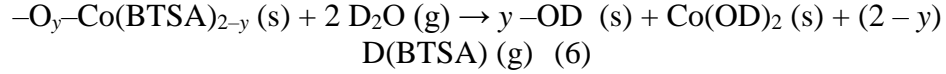
Net reaction:



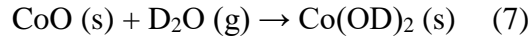
First half-reaction ($0 < y < 2$):



Second half-reaction ($0 < y < 2$):



The above half-reaction can be a direct formation of Co(OD)_2 or the deposition of CoO , i.e. the second half-reaction (6), and a subsequent hydrolysis:

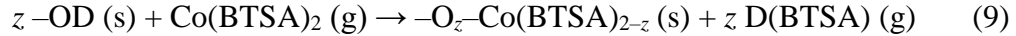


When taking in to account the reaction schemes that deposit CoO and Co(OH)_2 i.e. net reactions (1) and (4), we get the following combined scheme, where the final product is a combination of CoO and Co(OD)_2 :

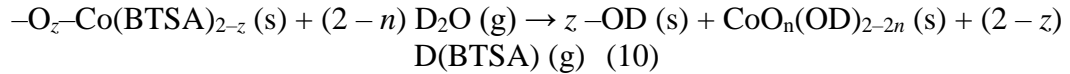
Net reaction ($0 < n < 1$):



First half-reaction ($0 < z < 1$):



Second half-reaction:



An important similarity between the Eqs. (1), (4) and (8) is that the interpretation of the QMS data in these reaction schemes is the same. This follows from the fact that we only measure the ratio of D(BTSA) released during the metal precursor pulse versus D(BTSA) released during the water pulse, and this ratio is the same in all the schemes (i.e. QMS cannot differentiate between the unknown stoichiometric coefficients x , y , and

z). In analyzing the measurement data, we interpret the results in terms of Eq. (10), i.e. we calculate a value for z.

The m/z values monitored during the *in-situ* reaction mechanism studies are listed in Table II. The m/z ratios of interest regarding the film deposition reaction mechanism are those belonging to THF⁺ (m/z = 72) and most intense peak of the deuterated BTSA ligand, D(BTSA) (m/z = 147).

TABLE 2. m/z values of reaction by-products monitored using QMS.

m/z	species	observed	notes
20	D ₃ N ⁺	no	molecular peak
72	C ₄ H ₈ O ⁺ (THF ⁺)	yes	molecular peak
75	DSi(CH ₃) ₃ ⁺	no	molecular peak
91	DOSi(CH ₃) ₃ ⁺ , D ₂ NSi(CH ₃) ₃ ⁺	no	molecular peak(s)
132	(H ₃ C) ₃ Si-Si(CH ₃) ₃ ⁺	yes	molecular peak
146	DN[Si(CH ₃) ₂] ₂ ⁺ , O[Si(CH ₃) ₂] ₂ ⁺	no	fragment(s)
147	DN[Si(CH ₃) ₃][Si(CH ₃) ₂] ⁺	yes	most intense peak of D(BTSA)
162	DN[Si(CH ₃) ₃] ₂ ⁺ , O[Si(CH ₃) ₃] ₂ ⁺	yes	molecular peaks(s)
233	N[Si(CH ₃) ₃] ₃ ⁺	no	molecular peak

Based on the QMS measurements, the THF ligand does not have a notable effect on the reaction mechanism. In the signal arising from THF, almost no difference is seen in the integrated signal intensities during the process pulses and the reference pulses (Fig. 8). This could be due to THF being separated from the parent molecule before reaching the surface, or a complete release of THF from the cobalt precursor upon adsorption on the surface, as THF signals are seen only during the Co(BTSA)₂(THF) pulses, and not

during the D₂O pulses. We note that Co(BTSA)₂(THF) can be purified via sublimation, during which the molecule evaporates intact as discussed in the precursor synthesis section. This indicates that during film deposition, THF is released from the parent cobalt precursor molecule only during the surface reactions. The passive role of THF is not surprising, as it is only an adduct forming ligand in the cobalt precursor. Because it has zero charge, it can simply dissociate from the cobalt precursor without any reaction with e.g. hydroxyl groups. Furthermore, THF is only a weak Lewis base, which makes it unlikely to adsorb on the surface at temperatures in which the film deposition and *in-situ* experiments are done. For these reasons, THF has not been included in calculations which are based on the QMS and QCM data.

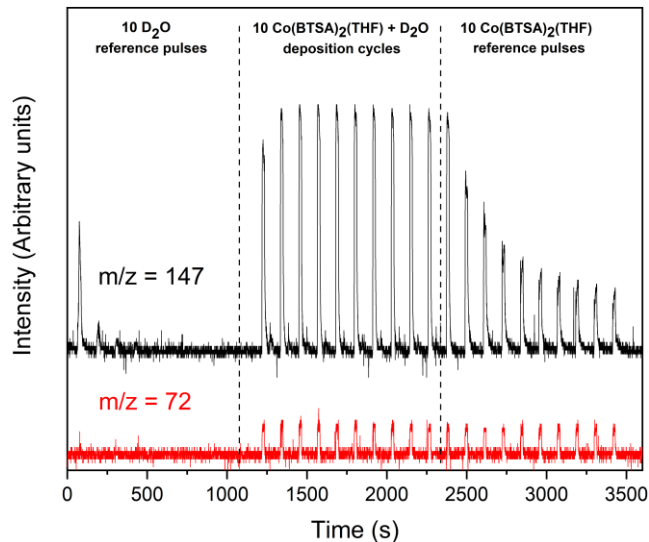


FIG 8. QMS data for $m/z = 72$ (THF⁺) and $m/z = 147$ (DN[Si(CH₃)]Si(CH₃)₂)⁺ at 100 °C.

In analyzing the QMS data, we integrate the signal intensities arising from D(BTSA) during the Co(BTSA)₂(THF) pulse and D₂O pulse, as these intensities are proportional to the amount of D(BTSA) released during the said pulses. From these integrated values, we subtract the integrated values of the same signals observed during

the respective reference pulses. We do not need to analyze the absolute values of the mass signals, as we are only interested in their ratio ($\equiv R$), referring to equations (9) and (10):

$$R = z / (2 - z) \quad (11)$$

Using a measured value of R , we can calculate z :

$$z = 2R / (1 + R) \quad (12)$$

The most notable aspect of the QMS data is that in all the experiments the great majority of $D(BTSA)$ ($m/z = 147$) is released during the $Co(BTSA)_2(THF)$ pulse. Calculating R from the data presented in Figs. 8 and 9 using numerical integration, we obtain $z \approx 1.90$. In fact, when the purge time after the $Co(BTSA)_2(THF)$ pulse is made long enough, only a weak signal from $D(BTSA)$ can be observed in the mass spectrum during the D_2O pulse (Fig. 9).

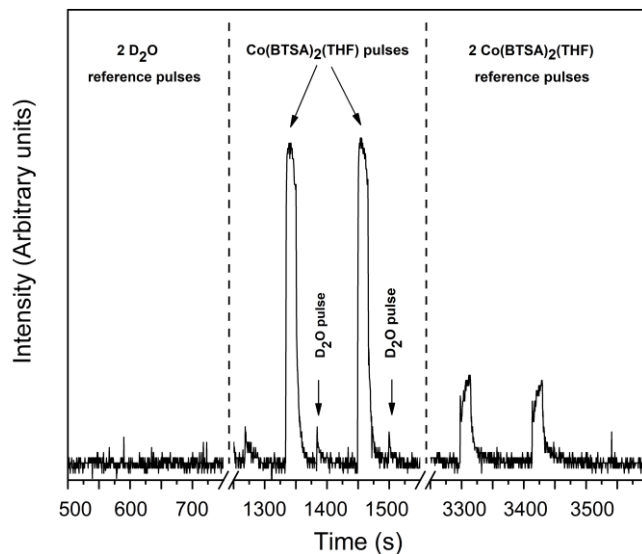
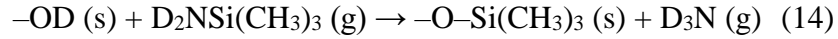
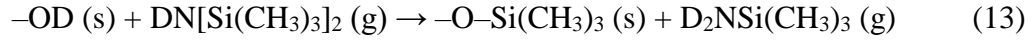
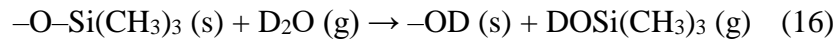
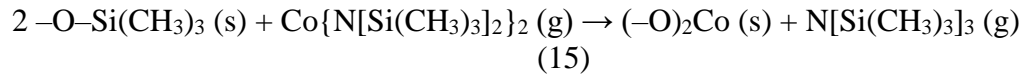


FIG 9. QMS data for $m/z = 147$ ($DN[Si(CH_3)][Si(CH_3)_2]^+$) at $100\text{ }^\circ\text{C}$ for two cycles of the $Co(BTSA)_2(THF) + D_2O$ process.

A complicating factor in the analysis of gaseous by-products are the following possible side-reactions between the released D(BTSA) and surface hydroxyl groups⁵⁹, which create surface methylsilyl groups:



If such methylsilyl groups were created, they could in principle be transformed to methylsilazane groups by the cobalt precursor, or back to hydroxyl groups by the following water pulse:



On the other hand, if the formation of surface methylsilyl groups was irreversible, they would provide some explanation for the silicon and carbon impurities seen in the films. However, the gaseous by-products from reactions (13–16) were not detected with QMS. If the proportion of such reactions relative to all the other reactions is small, the released by-products might not be detectable due to instrumental limitations. At any rate, a partial decomposition or condensation of the cobalt precursor seems to be a better explanation for the observed silicon and carbon impurities in the films, the latter being a more feasible explanation due to the low deposition temperature.

In addition to the QMS measurements, the cobalt oxide film deposition process was also studied using QCM, as it provides an independent mean to obtain an experimental value for z . In these measurements, the mass changes during the reference

pulses of both D_2O and $Co(BTSA)_2(THF)$ are of interest. During the D_2O reference pulses the mass increases in relatively large amounts, and then decreases during the following purge (Fig. 10).

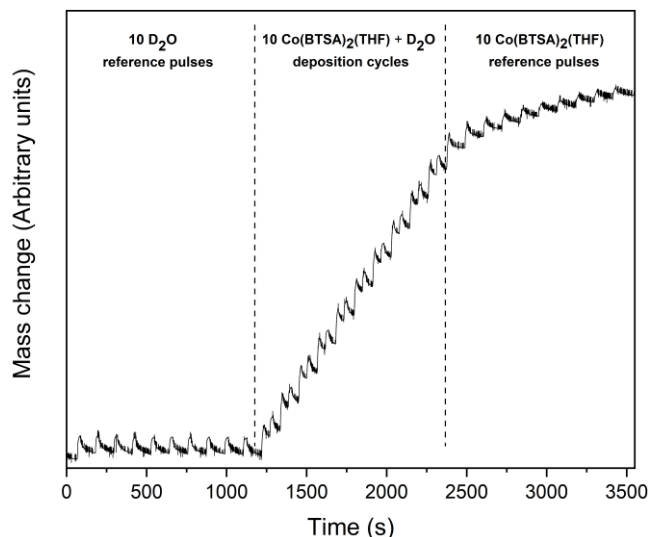
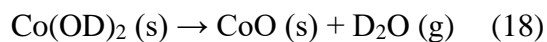
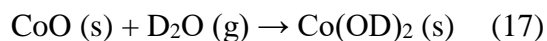


FIG 10. QCM data for the $Co(BTSA)_2(THF) + D_2O$ process at $100^\circ C$.

This effect could be due to simple physisorption/chemisorption and subsequent desorption, or due to hydroxylation (17) and subsequent dehydroxylation (18) of the underlying cobalt oxide:



During the $Co(BTSA)_2(THF)$ reference pulses the mass seems to change non-reversibly during each pulse. This could be due to physisorption or chemisorption with very slow desorption, or a very slowly saturation of $Co(BTSA)_2(THF)$ to the bulk of the

films. More likely explanations could be either a decomposition or a condensation of the precursor itself, or a very slow depletion of the surface –OD groups. As already stated earlier, condensation is much more likely than decomposition due to the low deposition temperature. Similar behavior has been observed in the *in-situ* QCM studies on the LiBTSA/O₃ ALD process.³⁵ However, as in the case of the LiBTSA + O₃ process study,³⁴ saturation tests based on thickness measurements seemed to indicate very good self-limiting behavior also in the case of the process reported herein. In the ALD process itself, the mass increases sharply at the very beginning of the Co(BTSA)₂(THF) pulses, with a slower, albeit significant, increase rate afterwards (Fig. 11).

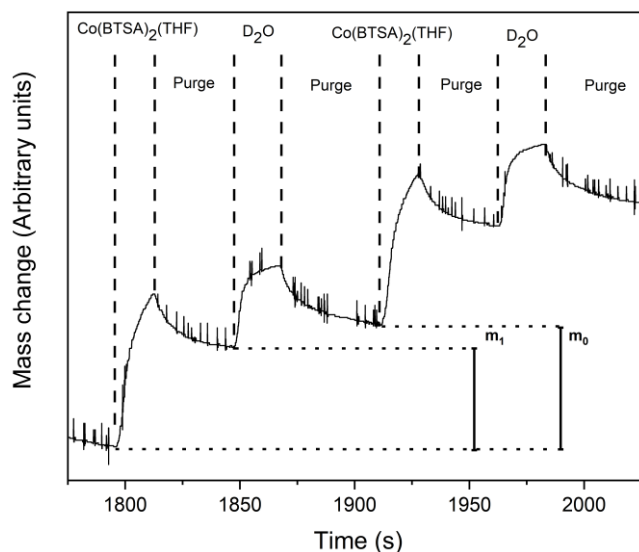


FIG 11. QCM data for the Co(BTSA)₂(THF) + D₂O process at 100°C.

During the following purge, the mass decreases approximately to a level which corresponds to the onset of the lower rate mass increase during the previous pulse. The mass increase does not seem to saturate even when using long pulses. Again, part of this effect can be due to condensation of the cobalt precursor. However, because the mass

also decreases during the following purge, there also seems to be some reversible physisorption of the precursor involved. During the ALD process, at the onset of the D₂O pulse the mass increases sharply, after which it saturates fairly quickly. During the following purge, an effect similar to the one seen during the D₂O reference pulses can be observed, as the mass decreases and approximately saturates again to a lower level.

The mass increase during the metal precursor pulse ($\equiv m_1$) equals the mass of the precursor vapor adsorbed on the surface minus the mass of gaseous by-products released:

$$m_1 = m(\text{Co}(\text{BTSA})_2) - z m(\text{D}(\text{BTSA})) \quad (19)$$

The mass increase after one whole ALD cycle ($\equiv m_0$) equals the mass of all gases adsorbed during the whole cycle minus the total mass of gaseous by-products released.

More simply, this is equal to the mass of the deposited film:

$$m_0 = m(\text{Co}(\text{BTSA})_2) - 2 m(\text{D}(\text{BTSA})) = m(\text{CoO}_n(\text{OD})_{2-2n}) \quad (20)$$

Similarly to the analysis of the QMS data, we do not need the absolute values of the mass increases, but instead the ratio of m_1 to m_0 :

$$m_1/m_0 = [m(\text{Co}(\text{BTSA})_2) - z m(\text{D}(\text{BTSA}))] / m(\text{CoO}_n(\text{OD})_{2-2n}) \quad (21)$$

Using the measured value of m_1/m_0 , we can calculate z :

$$z = [m(\text{Co}(\text{BTSA})_2) - (m_1/m_0) m(\text{CoO}_n(\text{OD})_{2-2n})] / m(\text{D}(\text{BTSA})) \quad (22)$$

Because the value of n in equation (22) is unknown, we calculate the extremum values of z for $0 < n < 1$, i.e. for the range of all possible n according to the scheme presented in Eqs. (8)–(10). From Fig. 11 we obtain an m_1/m_0 value of approximately 0.80, which corresponds to the following values for z :

$$z(n = 0) = [m(\text{Co}(\text{BTSA})_2) - (m_1/m_0) m(\text{Co}(\text{OD})_2)] / m(\text{D}(\text{BTSA})) \approx 1.86$$

$$z(n = 1) = [m(\text{Co}(\text{BTSA})_2) - (m_1/m_0) m(\text{CoO})] / m(\text{D}(\text{BTSA})) \approx 1.96$$

Both of these values are in good agreement with the value for z obtained using QMS and therefore, the QCM data can not give a definitive answer on how much of the mechanism involves the formation of pure cobalt(II) oxide as compared to cobalt(II) hydroxide.

To sum up the *in-situ* studies, the experimentally found value for z is close to 2, which suggests that the primary film-forming reaction mechanism at 100 °C is a reaction between one $\text{Co}(\text{BTSA})_2(\text{THF})$ molecule between two surface hydroxyl ($-\text{OD}$) groups and the subsequent release of two equivalents of $\text{D}(\text{BTSA})$. During the following D_2O pulse, one D_2O molecule reacts with the surface group that forms after the cobalt precursor pulse which leads to the formation of two new surface hydroxyl groups (Fig. 12). It is fairly exceptional that almost all of the ligands on average are released already during the metal pulse. This would indicate that the $\text{Co}(\text{BTSA})_2(\text{THF})$ or the $\text{Co}(\text{BTSA})_2$ molecule cannot strongly adsorb on the surface unless it loses hydrogenated BTSA ligands in reaction with hydroxyl groups.

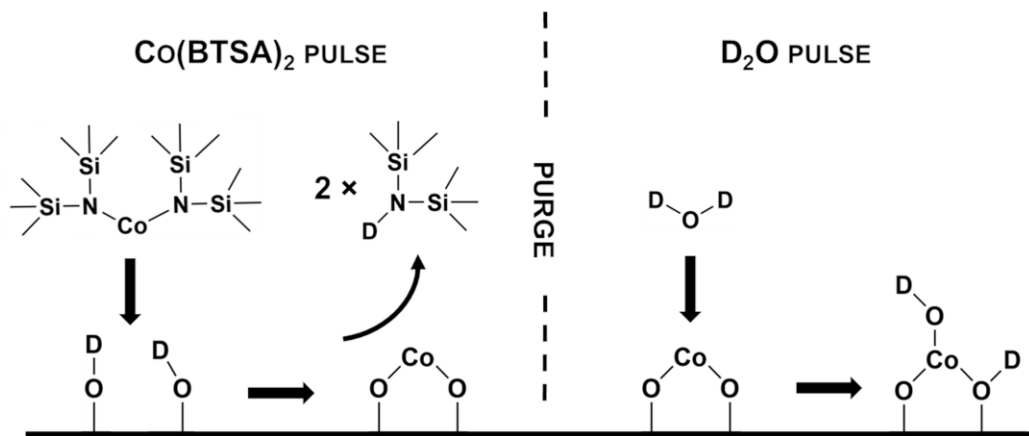


FIG. 12. Proposed reaction mechanism scheme for cobalt oxide film deposition for the $\text{Co}(\text{BTSA})_2(\text{THF}) + \text{D}_2\text{O}$ process at 100°C . The THF molecule of $\text{Co}(\text{BTSA})_2(\text{THF})$ has been omitted for clarity.

IV. SUMMARY AND CONCLUSIONS

In this study, we have described a new, low-temperature ALD process for cobalt oxide thin films using $\text{Co}(\text{BTSA})_2(\text{THF})$ and H_2O as precursors. The adduct forming THF ligand in the precursor molecule was found to have a passive role in the deposition process while at the same time, the inclusion of the adduct forming ligand enabled the cobalt precursor to be evaporated at a low temperature of 55°C . The deposition process exhibited good saturation behavior at deposition temperatures of 100 and 200°C and produced visually uniform films on $5 \times 5 \text{ cm}^2$ substrates. Film characterization showed that films deposited at low temperatures were more crystalline than the ones deposited at high temperatures, which is likely due to the increase of Si impurities at the higher temperatures. In addition to the decreased crystallinity, the incorporation of Si atoms from the BTSA ligands is also likely to be detrimental with respect to applications where stoichiometric and impurity-free cobalt monoxide is required. An *in-situ* QMS and QCM

study revealed that the most probable film-forming reaction mechanism at 100 °C is an exchange reaction between surface BTSA ligands and water, which produces volatile, hydrogenated BTSA as the main reaction by-product. The QCM measurements show also mass growth behavior which may imply partial condensation of the cobalt precursor. Regarding future studies, there is more research to be done on metal BTSA precursors, as they are relatively cheap and easy to synthesize. However, it should be emphasized that this family of metal precursors might lack some of the other characteristics of ideal ALD precursors, as they seem to be prone to condensation at low temperatures and partial thermal decomposition at higher temperatures.

ACKNOWLEDGMENTS

Financial support by The Finnish Centre of Excellence in Atomic Layer Deposition (Academy of Finland) and the EU-FP7 Grant “4G-PHOTO-CAT” (Grant No. 309636) are gratefully acknowledged. Mr. Eero Tirkkonen is thanked for his assistance in the film deposition and characterization experiments.

¹ J. Yang, H. Liu, W.N. Martens, and R.L. Frost, *J. Phys. Chem. C* **114**, 111 (2010).

² X. Zhang, Y.-S. Chen, P. V Kamat, and S. Ptasinska, *J. Phys. Chem. C* (2018).

³ M. Schwarz, F. Faisal, S. Mohr, C. Hohner, K. Werner, T. Xu, T. Skála, N. Tsud, K.C. Prince, V. Matolín, Y. Lykhach, and J. Libuda, *J. Phys. Chem. Lett.* **9**, 2763 (2018).

⁴ J.B. Gerken, J.G. McAlpin, J.Y.C. Chen, M.L. Rigsby, W.H. Casey, R.D. Britt, and S.S. Stahl, *J. Am. Chem. Soc.* **133**, 14431 (2011).

⁵ M. Favaro, J. Yang, S. Nappini, E. Magnano, F.M. Toma, E.J. Crumlin, J. Yano, and

- I.D. Sharp, *J. Am. Chem. Soc.* **139**, 8960 (2017).
- ⁶ D. Li, L.-X. Ding, S. Wang, D. Cai, and H. Wang, *J. Mater. Chem. A* **2**, 5625 (2014).
- ⁷ H. Kim, W.I. Choi, Y. Jang, M. Balasubramanian, W. Lee, G.O. Park, S. Bin Park, J. Yoo, J.S. Hong, Y.-S. Choi, H.S. Lee, I.T. Bae, J.M. Kim, and W.-S. Yoon, *ACS Nano* **12**, 2909 (2018).
- ⁸ B. Wang, J.B. Bates, F.X. Hart, B.C. Sales, R.A. Zuhr, and J.D. Robertson, *J. Electrochem. Soc.* **143**, 3203 (1996).
- ⁹ Z.X. Shen, J.W. Allen, P.A.P. Lindberg, D.S. Dessau, B.O. Wells, A. Borg, W. Ellis, J.S. Kang, S.J. Oh, I. Lindau, and W.E. Spicer, *Phys. Rev. B* **42**, 1817 (1990).
- ¹⁰ J.F. Liu, S. Yin, H.P. Wu, Y.W. Zeng, X.R. Hu, Y.W. Wang, G.L. Lv, and J.Z. Jiang, *J. Phys. Chem. B* **110**, 21588 (2006).
- ¹¹ W.S. Seo, J.H. Shim, S.J. Oh, E.K. Lee, N.H. Hur, and J.T. Park, *J. Am. Chem. Soc.* **127**, 6188 (2005).
- ¹² J.F. Liu, Y. He, W. Chen, G.Q. Zhang, Y.W. Zeng, T. Kikegawa, and J.Z. Jiang, *J. Phys. Chem. C* **111**, 2 (2007).
- ¹³ L. Qiao, H.Y. Xiao, H.M. Meyer, J.N. Sun, C.M. Rouleau, A.A. Puretzky, D.B. Geohegan, I.N. Ivanov, M. Yoon, W.J. Weber, and M.D. Biegalski, *J. Mater. Chem. C* **1**, 4628 (2013).
- ¹⁴ J. Chen, X. Wu, and A. Selloni, *Phys. Rev. B* **83**, 245204 (2011).
- ¹⁵ W.L. Smith and A.D. Hobson, *Acta Crystallogr. Sect. B* **29**, 362 (1973).
- ¹⁶ M. Schwarz, S. Mohr, C. Hohner, K. Werner, T. Xu, and J. Libuda, *J. Phys. Chem. C* (2018).
- ¹⁷ M.C. Biesinger, B.P. Payne, A.P. Grosvenor, L.W.M. Lau, A.R. Gerson, and R.S.C.

- Smart, Appl. Surf. Sci. **257**, 2717 (2011).
- ¹⁸ S.M. George, Chem. Rev. **110**, 111 (2010).
- ¹⁹ R.W. Johnson, A. Hultqvist, and S.F. Bent, Mater. Today **17**, 236 (2014).
- ²⁰ V. Miikkulainen, M. Leskelä, M. Ritala, and R.L. Puurunen, J. Appl. Phys. **113**, 21301 (2013).
- ²¹ M.E. Donders, H.C.M. Knoops, M.C.M. van de Sanden, W.M.M. Kessels, and P.H.L. Notten, ECS Trans. **25**, 39 (2009).
- ²² K.B. Klepper, O. Nilsen, and H. Fjellvåg, J. Cryst. Growth **307**, 457 (2007).
- ²³ M. Diskus, O. Nilsen, and H. Fjellvag, Chem. Vap. Depos. **17**, 135 (2011).
- ²⁴ B. Han, K.H. Choi, J.M. Park, J.W. Park, J. Jung, and W.-J. Lee, J. Vac. Sci. Technol. A **31**, 01A145 (2013).
- ²⁵ B. Han, K.H. Choi, K. Park, W.S. Han, and W.-J. Lee, Electrochem. Solid State Lett. **15**, D14 (2012).
- ²⁶ D.K. Nandi, J. Manna, A. Dhara, P. Sharma, and S.K. Sarkar, J. Vac. Sci. Technol. A **34**, 01A115 (2016).
- ²⁷ J. Kim, T. Iivonen, J. Hämäläinen, M. Kemell, K. Meinander, K. Mizohata, L. Wang, J. Räisänen, R. Beranek, M. Leskelä, and A. Devi, Chem. Mater. **29**, 5796 (2017).
- ²⁸ D.J. Hagen, T.S. Tripathi, and M. Karppinen, Dalt. Trans. **46**, 4796 (2017).
- ²⁹ K.B. Klepper, O. Nilsen, and H. Fjellvag, Thin **515**, 7772 (2007).
- ³⁰ B.S. Lim, A. Rahtu, and R.G. Gordon, Nat. Mater. **2**, 749 (2003).
- ³¹ T.Q. Ngo, A. Posadas, H. Seo, S. Hoang, M.D. McDaniel, D. Utess, D.H. Triyoso, C. Buddie Mullins, A.A. Demkov, and J.G. Ekerdt, J. Appl. Phys. **114**, 84901 (2013).
- ³² K. Väyrynen, T. Hatanpää, M. Mattinen, M. Heikkilä, K. Mizohata, K. Meinander, J.

- Räisänen, M. Ritala, and M. Leskelä, *Chem. Mater.* **30**, 3499 (2018).
- ³³ D. V. Baxter, M.H. Chisholm, G.J. Gama, A.L. Hector, and I.P. Parkin, *Chem. Vap. Depos.* **1**, 49 (1995).
- ³⁴ J. Hämäläinen, F. Munnik, T. Hatanpää, J. Holopainen, M. Ritala, and M. Leskelä, *J. Vac. Sci. Technol. A* **30**, 01A106 (2012).
- ³⁵ Y. Tomczak, K. Knapas, M. Sundberg, M. Leskelä, and M. Ritala, *J. Phys. Chem. C* **117**, 14241 (2013).
- ³⁶ E. Østreng, H.H. Sønsteby, T. Sajavaara, O. Nilsen, and H. Fjellvåg, *J. Mater. Chem. C* **1**, 4283 (2013).
- ³⁷ M. Vehkamäki, T. Hatanpää, M. Ritala, and M. Leskelä, *J. Mater. Chem.* **14**, 3191 (2004).
- ³⁸ S. Selvaraj, H. Moon, J.Y. Yun, and D.H. Kim, *Korean J. Chem. Eng.* **33**, 3516 (2016).
- ³⁹ J. Tupala, M. Kemell, M. Mattinen, K. Meinander, S. Seppälä, T. Hatanpää, J. Räisänen, M. Ritala, and M. Leskelä, *J. Vac. Sci. Technol. A* **35**, 041506 (2017).
- ⁴⁰ W. He, S. Schuetz, R. Solanki, J. Belot, and J. McAndrew, *Electrochem. Solid-State Lett.* **7**, G131 (2004).
- ⁴¹ D.H. Triyoso, R.I. Hegde, J. Grant, P. Fejes, R. Liu, D. Roan, M. Ramon, D. Werho, R. Rai, L.B. La, J. Baker, C. Garza, T. Guenther, B.E. White, and P.J. Tobin, *J. Vac. Sci. Technol. B* **22**, 2121 (2004).
- ⁴² D.H. Triyoso, R.I. Hegde, J.M. Grant, J.K. Schaeffer, D. Roan, B.E. White, and P.J. Tobin, *J. Vac. Sci. Technol. B* **23**, 288 (2005).
- ⁴³ K. Kukli, M. Ritala, T. Pilvi, T. Sajavaara, M. Leskelä, A.C. Jones, H.C. Aspinall, D.C. Gilmer, and P.J. Tobin, *Chem. Mater.* **16**, 5162 (2004).

- ⁴⁴ K. Kukli, M. Ritala, V. Pore, M. Leskelä, T. Sajavaara, R.I. Hegde, D.C. Gilmer, P.J. Tobin, A.C. Jones, and H.C. Aspinall, *Chem. Vap. Depos.* **12**, 158 (2006).
- ⁴⁵ W.-H. Nam and S.-W. Rhee, *Electrochem. Solid-State Lett.* **7**, C55 (2004).
- ⁴⁶ J.P. Coyle, G. Dey, E.R. Sirianni, M.L. Kemell, G.P.A. Yap, M. Ritala, M. Leskelä, S.D. Elliott, and S.T. Barry, *Chem. Mater.* **25**, 1132 (2013).
- ⁴⁷ M. Mäkelä, T. Hatanpää, M. Ritala, M. Leskelä, K. Mizohata, K. Meinander, and J. Räisänen, *J. Vac. Sci. Technol. A* **35**, 01B112 (2016).
- ⁴⁸ K. Knapas and M. Ritala, *Crit. Rev. Solid State Mater. Sci.* **38**, 167 (2013).
- ⁴⁹ A.M. Bryan, G.J. Long, F. Grandjean, and P.P. Power, *Inorg. Chem.* **52**, 12152 (2013).
- ⁵⁰ T. Suntola, *Thin Solid Films* **216**, 84 (1992).
- ⁵¹ A. Rahtu and M. Ritala, *Proc. Electrochem. Soc.* **2000–13**, 105 (2000).
- ⁵² M. Ylilampi and T. Ranta-aho, *Thin Solid Films* **232**, 56 (1993).
- ⁵³ J. Jokinen, J. Keinonen, P. Tikkanen, A. Kuronen, T. Ahlgren, and K. Nordlund, *Nucl. Instruments Methods Phys. Res. Sect. B* **119**, 533 (1996).
- ⁵⁴ V. Pore, A. Rahtu, M. Leskelä, M. Ritala, T. Sajavaara, and J. Keinonen, *Chem. Vap. Depos.* **10**, 143 (2004).
- ⁵⁵ M.D. Groner, F.H. Fabreguette, J.W. Elam, and S.M. George, *Chem. Mater.* **16**, 639 (2004).
- ⁵⁶ M. Putkonen, T. Sajavaara, L. Niinistö, and J. Keinonen, *Anal. Bioanal. Chem.* **382**, 1791 (2005).
- ⁵⁷ F. Weinhold and R. West, *Organometallics* **30**, 5815 (2011).
- ⁵⁸ Y. Hou, H. Kondoh, M. Shimojo, T. Kogure, and T. Ohta, *J. Phys. Chem. B* **109**, 19094 (2005).

⁵⁹ S. Haukka and A. Root, *J. Phys. Chem.* **98**, 1695 (1994).